Optimal design of a hybrid electric propulsive system for an anchor handling tug supply vessel

Zhu Jianyun, Chen Li*, Wang Bin, Xia Lijuan

State Key Laboratory of Ocean Engineering of Shanghai Jiao Tong University, Collaborative Innovation Center for Advanced Ship and Deep-Sea Exploration, Shanghai 200240, China

HIGHLIGHTS

- Multi-objective optimization is proposed by considering fuel economy, emission and cost.
- Optimal sizing of a hybrid diesel/battery/shore power system is obtained by NSGA-II.
- Performance tests are conducted on a real-time hardware-in-the-loop platform.

ABSTRACT

Hybrid electric propulsive systems (HEPSs) attract increasing research interest due to their environmental and economic merits. However, the design optimization of HEPSs with the single objective of fuel saving may result in increased greenhouse gas (GHG) emission and high cost. The present study proposes a multi-objective optimization method to obtain an optimal trade-off with respect to fuel consumption, GHG emission, and lifecycle cost. Due to high convergence in solving constrained multi-objective optimization problems, the non-dominated sorting genetic algorithm II (NSGA-II) is developed to explore an optimal design space. Performance tests are conducted on a real-time hardware-in-the-loop (HIL) platform. The hybrid diesel/battery/shore power system on an anchor handling tug supply vessel is considered as a study case. The results of the proposed NSGA-II are compared with those from a single-objective optimization pursuing minimum fuel consumption. The proposed method outputs designs that can significantly reduce GHG emission and lifecycle cost by sacrificing low fuel consumption when compared with that of single objective optimization. Furthermore, the HEPS designed by the proposed method exhibits advantages over the conventional propulsive system in terms of all the three aspects.

1. Introduction

With respect to the challenges of petroleum exhaustion and global warming, international regulations, such as the energy efficiency design index (EEDI) and ship energy efficiency management plan (SEEMP), were enacted to a decrease the growth rate of fuel consumption and greenhouse gas (GHG) emission in the shipping industry [1]. Thus, the requirement of developing energy-efficient and environment-friendly ships resulted in the development of several types of hybrid propulsion and power supply architectures [2–4]. Among them, hybrid electric propulsive systems (HEPSs) attract significant academic interest due to their potential for fuel saving and GHG emission reduction in part load and dynamic load operation, which are commonly required by off-shore vessels such as anchor handling tug supply vessels (AHTSs) [5–8].

Since HEPSs are characterized by two or more power sources that

bring an additional degree of freedom that allows for more efficient operation, design optimization is required to clarify the economic and environmental merits of HEPSs [9–11]. However, in previous studies, the optimization was performed only with the goal of fuel saving while GHG emission and lifecycle cost were not considered in the objective function [12,13]. In [12], an optimization approach was proposed to maximize the overall propulsive efficiency of a submarine system. A solution involving the tradeoff between high-speed performance and low-speed performance was determined. In [13], a HEPS was optimized for a medium-size boat by considering the objective of minimum fuel consumption. The simulation results indicated that a HEPS leads to 40% reduction in fuel consumption when compared to that of a conventional propulsive system. However, fuel saving does not necessarily mean low GHG emission and generally requires additional equipment investment that increases cost. Specifically, GHG emission reduction is a major

reason for the implementation of HEPSs, and the lifecycle cost determines the economic feasibility of the widespread application of HEPSs. Thereafter, it is important to examine a multi-objective optimization design that achieves a compromise with respect to the fuel consumption, GHG emission, and lifecycle cost.

Multi-objective optimization can obtain better designs in terms of comprehensive performance when compared with the single-objective optimization [9,14]. Specifically Lan et al. demonstrated the cost and emission for four cases designed by the three-objective optimal method for a hybrid photovoltaic (PV)/diesel/battery system in a ship [9]. It is observed that the optimization only accounts for the power provided for the non-propulsive load without considering the power for the propulsive load. Optimization with respect to two of the three objectives (i.e., minimization of fuel consumption, GHG emission, and cost) of hybrid urban buses was performed by Ribau et al. by using a vehicle simulation software ADVISOR [14]. The results indicated that the two-objective optimizations exhibit clear advantages over the single-objective optimizations. Nevertheless, a more comprehensive optimization that simultaneously considers fuel consumption, GHG emission, and lifecycle cost was not explored. On the other hand, significant differences are observed between the hybrid vehicles and HEPS vessels. First, long range and durable endurance is essential for HEPS vessels while hybrid vehicles can be refilled, recharged, or conveniently repaired. Furthermore, relatively large non-propulsive power is commonly required in HEPS vessels to drive working devices, such as cranes, radars, and laser weapons, while the auxiliary power requirement of hybrid vehicles is relatively low. Additionally, HEPS vessels typically use multiple gensets or even multiple types of prime movers that are connected to a common power bus and independently controlled while the hybrid vehicles typically use a set of power devices. Finally, in contrast to hybrid vehicles that are likely to stop-and-go frequently, HEPS vessels typically keep sailing in a mode for a long time with a relatively stable power requirement, and it is inefficient to apply regenerative braking technology due to the lack of direct adhesion between the propeller and water [15].

Several algorithms that address the multi-objective optimization problem were examined and recently developed in various applications. The adaptive simulated annealing genetic algorithm (ASAGA) was developed by Hui et al. to develop a bi-objective optimal design for minimal fuel consumption and maximal dynamic performance of a hydraulic hybrid vehicle [16]. The ASAGA aggregates all objectives into a single objective formulation by introducing weighting factors. The disadvantage is that inappropriate weighting factors can deteriorate the performance of the optimization, and thus the selection of the weighting factors is a challenging issue. A Pareto optimal solution set provides an effective method to deal with multi-objective optimal problems as opposed to using the weighting factors. Thus, a family of multi-objective ant colony optimization (MOACO) algorithms was designed by Mora et al. to solve a pathfinding problem for a military unit by considering the objectives of maximum speed and safety [17]. However, the MOACO always involves a long period to reach convergence and tends to be confined to the local optimum solution. Several advanced multi-objective optimizations were examined with the aim of overcoming the disadvantages of the MOACO. For example, a multi-objective particle swarm optimization algorithm (MOPSO) was developed by Borhanazad et al. to optimally design a hybrid micro-grid system involving diesel generators, wind turbines, PV panels, and batteries [18]. A non-dominated sorting genetic algorithm II (NSGA-II) was developed by Ahmadi et al. to design a solar-based multi-generation energy system that is targeted at improving the cost rate and exergy efficiency [19]. A comparison between the MOPSO and NSGA-II was examined by Ghodratnama et al. to solve a multi-objective multi-route flexible flow line problem [20]. Results indicated that the NSGA-II provides better results in terms of space and quality criteria although it provides fewer Pareto solutions. Furthermore, the NSGA-II is insensitive to initial values [21] and is proven as efficient for the sizing of power

systems [22]. In order to explore effective design space, both the NSGA-II and MOPSO are developed for optimal design in the present study. Their Pareto solution sets are compared for the convenience of locating the optimal solution.

The present study proposes a multi-objective optimization methodology for the optimal design of HEPSs by considering the comprehensive goal of simultaneously minimizing fuel consumption, GHG emission, and lifecycle cost. Five sizing parameters and two energy management parameters are considered as the optimization variables. The Pareto solution sets calculated from the NSGA-II and MOPSO are compared. The optimal design is selected from the Pareto sets. A 120-ton bollard pull AHTS is considered as a study case. The performance tests are performed on a hardware-in-the-loop (HIL) platform. In order to highlight the advantage and significance of the multi-objective optimization, the results of the multi-objective optimization are compared with those from a single-objective optimization by only focusing on minimum fuel consumption as well as those from the conventional propulsive system.

The contributions of the present study can be summarized as follows.

(1). When compared with the conventional single-objective optimization that only focuses on minimum fuel consumption, multi-objective optimization is proposed for the design of HEPSs by introducing two additional objectives, namely GHG emission and lifecycle cost. Minimum fuel consumption does not necessarily mean low GHG emission and low lifecycle cost, and thus multi-objective optimization can be more significant for industrial applications.

(2). The NSGA-II is developed to explore an effective design space. The Pareto solution set is compared with that from the MOPSO in terms of the space criteria and quality criteria.

(3). A real-time HIL platform is developed to test the performance of HEPSs. The platform is flexible because its program can be modified to fit different configurations and working conditions.

The present study is organized as follows: Section 2 constructs mathematical models for the HEPS. Section 3 describes the energy management strategy. Section 4 presents the optimal algorithm. Section 5 provides the results and discussion. Finally, Section 6 presents the conclusions.

2. Mathematical modeling

In the conventional propulsive system with twin propellers as shown in Fig. 1(a), two diesel engines (propulsive engine) drive two propellers through two gearboxes. Additionally, two gensets are connected to a power bus to provide non-propulsive load including the hotel load and operational load. Comparatively, in the HEPS as shown in Fig. 1(b), two motors drive the two propellers through two gearboxes. The propulsive load (required by the motors) and non-propulsive load are fed by electric power from an integrated power bus. The power bus coordinates the storage and utilization of the electricity from the two gensets, battery pack, and shore power plant based on appropriate energy management strategies. Therefore, the examined HEPS is termed as the hybrid diesel/battery/shore power system. The differences between the HEPS and its conventional benchmark are summarized in Table 1. In order to facilitate design optimization, the modeling of the HEPS is given as follows.

2.1. Diesel engines

The two diesel engines in the examined HEPs are identical. The energy management strategy determines whether or not each of the two engines works. A scalable model is constructed for each engine by using the Willans line method [23,24]. The method defines the break mean

(a) conventional propulsive system

(b) HEPS

Mechanical Connection —— Electric Connection —— Gearbox

Generator (G) Motor (M) Propeller

Diesel engine ⬚OOOO⬚ Genset ⬚OOOO⬚-(G)
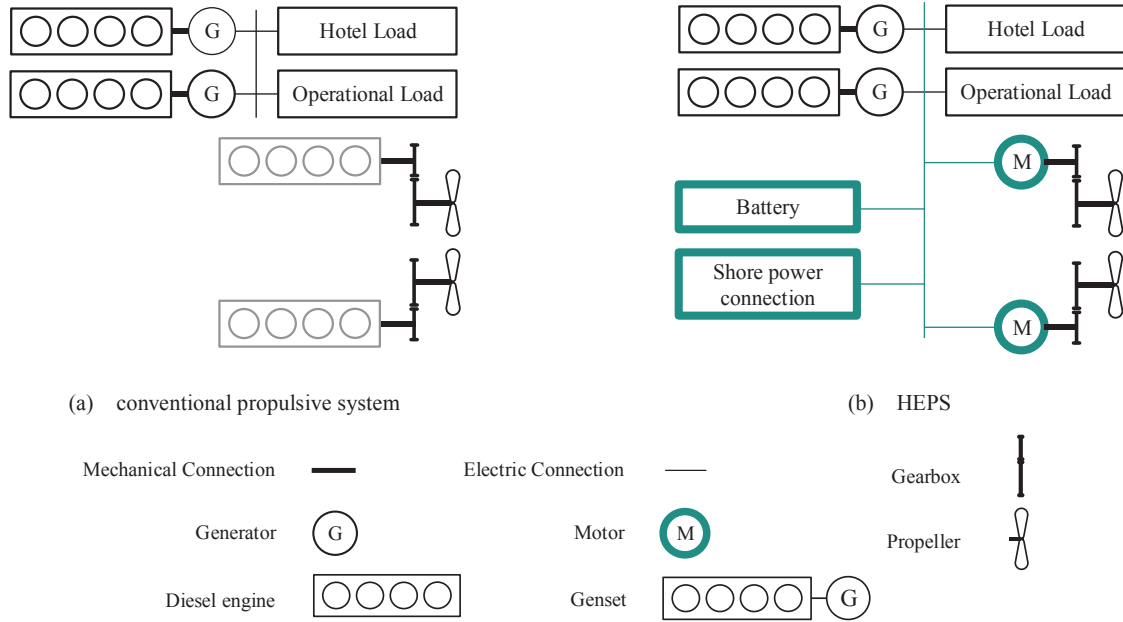
Fig. 1. Diagram of propulsive systems.

Table 1
Differences between the conventional propulsive system and HEPS.

Item	Conventional propulsive system	HEPS
Propellers driven by	Diesel engines	Motors
Number of diesel engines	4	2
Battery	None	Yes
Shore power connection	None	Yes

effective pressure (*BMEP*) and available mean effective pressure (*AMEP*) of a diesel engine as follows.

$$BMEP = T_d \cdot \frac{4\pi}{V_d} \quad (1)$$

$$AMEP = H_{LHV} \cdot \frac{4\pi}{V_d} \frac{\dot{m}_f}{\omega_d} \quad (2)$$

where T_d, V_d, and ω_d denote the output torque, displacement, and rotating velocity of the diesel engine, respectively; and $H_{LHV} \dot{m}_f$ denote the lower heating value and mass flow of the fuel, respectively.

Based on the Willans line method, the two pressures, namely *BMEP* and *AMEP*, are fitted by a polynomial as follows [23,24]:

$$BMEP = [e_0 - e_1 \cdot AMEP] \cdot AMEP - P_{loss} \quad (3)$$

in which,

$$e_0 = e_{00} + e_{01} v_p + e_{02} v_p^2 \quad (4)$$

$$e_1 = e_{10} + e_{11} v_p \quad (5)$$

$$P_{loss} = e_{p0} + e_{p2} \cdot v_p^2 \quad (6)$$

$$v_p = \frac{S_d}{\pi} \omega_d \quad (7)$$

$$S_d = \frac{4}{\pi} \frac{V_d}{B_d^2} \quad (8)$$

where P_{loss} denotes the mean effective pressure loss, v_p denotes the average piston speed, S_d denotes the piston stroke, B_d denotes the piston bore, and $e_0, e_{00}, e_{01}, e_{02}, e_1, e_{10}, e_{11}, e_{p0}$, and e_{p2} denote the Willans line coefficients that are inherited by the new designed diesel engine that belongs to the same class as the baseline diesel engine based on extant

studies [23,24].

Therefore, given the data of *BMEP* and *AMEP* of a baseline diesel engine, the Willans line coefficients are obtained by parameter identification from (3). Thereafter, given the effective torque T_d, displacement V_d, and stroke S_d of a new diesel engine, *BMEP* is calculated from (1); following that *AMEP* is calculated by solving the Eq. (3); finally, the mass flow $\dot{m}_f$ is calculated from (2). Thus, the mass flow $\dot{m}_f$ of a class of diesel engine designs is obtained.

2.2. Generators

The two generators are identical. The energy management strategy determines whether or not each of the two engines works. The output power P_G of each generator is calculated as follows.

$$P_G = \eta_{gen} T_d \omega_d \quad (9)$$

where η_{gen} denotes the generator efficiency.

2.3. Battery

Given the advantages of high energy density and flat characteristic of the voltage curve [25], the lithium-ion battery is adopted in the HEPS. The battery package consists of several battery modules that are connected in series. Each battery module consists of 40 battery cells that are connected in parallel. The number of battery modules, n_{ser}, should be designed. With respect to its application to the analysis of other hybrid powertrains, the Rint model is used to describe the current I_{bat} of the battery cell as follows [26–29].

$$I_{bat} = \frac{V_{oc}}{2R_{bat}} - \sqrt{\left(\frac{V_{oc}}{2R_{bat}}\right)^2 - \frac{P_{bat}}{R_{bat}}} \quad (10)$$

where V_{oc}, R_{bat}, and P_{bat} denote the open-circuit voltage, internal resistance, and terminal power of the battery cell respectively. Ignoring the imbalance of the battery cells, the current of the battery module is identical to that of the battery cell.

The state of charge (*SOC*) of a battery cell is calculated from an extant study as follows [26]:

$$SOC = SOC_0 - \int \frac{I_{bat} \eta_{colm}}{Q_{bat}} \quad (11)$$

where SOC_0 denotes the initial SOC, η_{colm} denotes the coulombic efficiency, and Q_{bat} denotes the battery capacity.

2.4. Motors

The two motors are identical. In the study, their working points are always identical. A scalable model is constructed for each motor by using the Willans line method [24]. The method defines two virtual pressures that are similar to $BMEP$ and $AMEP$ of the diesel engine model. The two virtual pressures of a motor are expressed as follows.

$$BMEP_M = \frac{T_m}{2V_r} \tag{12}$$

$$AMEP_M = \frac{P_{in}}{2V_r\omega_r} \tag{13}$$

where T_m denotes the output torque, P_{in} denotes the input electric power, ω_r denotes the rotating velocity, and V_r denotes the volume of the rotor. The calculation of V_r is given as follows:

$$V_r = \frac{1}{4}l_m d_m^2 \tag{14}$$

where l_m denotes the length of the rotor, and d_m denotes the diameter of the rotor.

Based on the Willans line method, the two virtual pressures, $BMEP_M$ and $AMEP_M$, are fitted by a polynomial as follows [23,24].

$$BMEP_M = [e_0 - e_1 \cdot AMEP_M] \cdot AMEP_M - P_{loss} \tag{15}$$

in which,

$$e_0 = e_{00} + e_{01}v_m + e_{02}v_m^2 \tag{16}$$

$$e_1 = e_{10} + e_{11}v_m \tag{17}$$

$$P_{loss} = e_{p0} + e_{p2} \cdot v_m^2 \tag{18}$$

$$v_m = \frac{1}{2}d_m\omega_m \tag{19}$$

where P_{loss} denotes the virtual mean effective pressure loss, v_m denotes the average line speed of the rotor, and e_0, e_{00}, e_{01}, e_{02}, e_1, e_{10}, e_{11}, e_{p0}, and e_{p2} denote the Willans line coefficients that are similar to those in (3).

2.5. Gearboxes

The two gearboxes are identical. In the study, their inputs and outputs are always identical. Each gearbox connects a motor and a propeller.

$$\omega_r = \frac{2\pi i}{60}n \tag{20}$$

$$T_m = \frac{1}{i\eta_{gear}}Q \tag{21}$$

where T_m denotes the output of motor, i denotes the gear ratio, n denotes the rotating velocity of the propeller, η_{gear} denotes the efficiency of gearbox, and Q denotes the effective torque of the propeller.

2.6. Propellers

The two propellers are identical. They operate collectively to carry the ship forward. In the study, their working points are always identical. For each propeller, the thrust force T and torque Q are calculated by the following formulae [12]:

$$T = K_T n^2 D^4 \rho \tag{22}$$

$$Q = K_Q n^2 D^5 \rho \tag{23}$$

where D denotes the propeller diameter, and K_T and K_Q denote the thrust and torque coefficient, respectively.

The values of K_T and K_Q are calculated as follows [12]:

$$K_T = K_{T1}\left(\frac{V}{nD}\right)^2 + K_{T2}\left(\frac{V}{nD}\right) + K_{T3} \tag{24}$$

$$K_Q = K_{Q1}\left(\frac{V}{nD}\right)^2 + K_{Q2}\left(\frac{V}{nD}\right) + K_{Q3} \tag{25}$$

where K_{T1}, K_{T2}, and K_{T3} denote the three thrust factors, and K_{Q1}, K_{Q2}, and K_{Q3} denote the three torque factors.

2.7. Ship dynamics

The longitudinal dynamics of the AHTS vessel is formulated as follows [30]:

$$N_p T(1-t_1) - F_{total} = m\frac{dv}{dt} \tag{26}$$

where N_p denotes the number of propellers, F_{total} denotes the total resistance, v denotes the velocity of the vessel, and m denotes the mass of the vessel. The thrust deduction coefficient, t_1, is calculated as follows [30]:

$$t_1 = 0.325C_B - 0.1885\frac{D}{\sqrt{Bd}} \tag{27}$$

where C_B denotes the bulbous bow resistance coefficient, D denotes the propeller diameter, and B and d denote the breadth and draught of the vessel, respectively.

2.8. Resistance

The total resistance F_{total} is calculated as follows [13,30,31]:

$$F_{total} = F_F(1 + k_1) + F_{APP} + F_W + F_B + F_{TS} + F_A \tag{28}$$

where F_F, F_{APP}, F_W, F_B, F_{TS}, and F_A denote the frictional resistance, appendage resistance, wave-making and wave-breaking resistance, additional pressure resistance of bulbous bow near the water surface, additional pressure resistance of immersed transom stem, and model-ship correlation resistance, respectively. The calculations are given as follows:

$$F_F = \frac{1}{2}\rho v^2 S(C_F + \Delta C_F) \tag{29}$$

$$1 + k_1 = c_{11}\{0.93 + c_{12}(B/L_R)^{0.92497}(0.95 - C_P)^{-0.521448}(1 - C_P + 0.0225l_{cb})^{0.6906}\} \tag{30}$$

$$F_{APP} = \frac{1}{2}\rho v^2 S_{APP}(1 + k_2)_{eq}C_F + \rho V^2\pi d^2 C_{BTT} \tag{31}$$

$$F_W = \frac{1}{2}\rho v^2 S C_W \tag{32}$$

$$F_B = \frac{1}{2}\rho v^2 S C_B \tag{33}$$

$$F_{TS} = \frac{1}{2}\rho v^2 S C_{TS} \tag{34}$$

$$F_A = \frac{1}{2}\rho v^2 S C_A \tag{35}$$

where C_A, C_B, C_F, ΔC_F, C_{BTT}, C_P, C_{TS}, and C_W denote the six coefficients; c_{11} and c_{12} denote the after-body shape factor and draught factor, respectively; ρ denotes the density of the sea-water; d denotes the draught of the vessel; S and S_{APP} denote the wet-surface area of the hull and appendage, respectively; L_R denotes the length coefficient, and l_{cb} denotes the longitudinal position of buoyant center. The factors $(1 + k_1)$ and $(1 + k_2)$ represent the form factor of viscous resistance of the hull and appendage resistance, respectively.
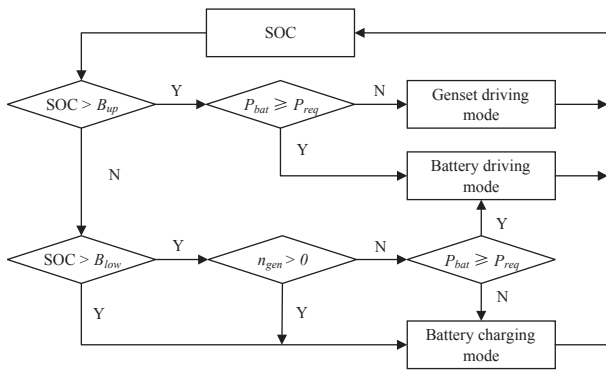
Fig. 2. Scheme of the mode switching strategy.

3. Energy management strategy

The rule-based energy management strategy is widely applied in the energy management of hybrid electric propulsive systems given its simplicity and reliability [32]. In the study, a rule-based strategy is developed to cooperate the usage of the electricity from the gensets, battery, and shore power plant with the aim of fulfilling the power required by the propellers, hotel load, and operational load of the HEPS. By using the strategy, the HEPS operates in three modes, namely the battery driving mode, genset driving mode, and battery charging mode. Given that most of the voyages of AHTS vessels are less than 24 h, the battery is charged to an initial amount that is denoted as SOC_0, before the vessel starts its one-day-voyage. During the voyage, the mode switching strategy is shown in Fig. 2 where P_{bat} denotes the maximum output power of the battery, P_{req} denotes the total power demand of the HEPS containing the propulsive and non-propulsive load, n_{gen} denotes the number of working gensets, and B_{up} and B_{low} denote the upper and lower bounds of SOC, respectively.

3.1. Battery driving mode

Based on the mode switching strategy, the battery driving mode works under the following two cases: (1) the battery SOC exceeds B_{up} and the power capacity P_{bat} of the battery exceeds the total power demand P_{req}; and (2) the battery SOC is between B_{up} and B_{low}, no genset is working, and P_{bat} exceeds P_{req}. In the battery driving mode, the total demanded power is supplied by the battery, and the two gensets are

shut down as shown in Fig. 3(a). Thus, the battery SOC gradually decreases. Here, P_E denotes the output power of the battery, and P_G denotes the output power of each working genset.

3.2. Genset driving mode

The genset driving mode works when the following two conditions are satisfied: (1) the power capacity P_{bat} of the battery is less than the total power demand P_{req}; and (2) it is not necessary to charge the battery because the SOC exceeds B_{up}. In the genset driving mode, the number of the working gensets should be selected based on the total power demand P_{req} and the rated output power P_{gen} of each genset as shown in Fig. 3(b). If $P_{gen} > P_{req}$, then a genset works and the other one is at rest and otherwise two gensets work.

3.3. Battery charging mode

During the voyage, the battery charging mode works when the following two conditions are satisfied: (1) the rated power P_{gen} of the genset exceeds the power demand P_{req}; (2) the battery SOC is less than B_{up}. In the battery charging mode, the gensets are operated within the rated working area and additional power is charged to the battery. In the mode, the number of the working gensets is selected based on the total power demand P_{req} and the rated output power P_{gen} of each genset as shown in Fig. 3(c). If $P_{gen} > P_{req}$, then a genset works and the other one is at rest; and otherwise two gensets work.

4. Optimal design

4.1. Optimization variables

Generally, the maximum output power of the diesel engines and motors are selected as the optimization variables in the optimal design for hybrid electric ships [13]. The disadvantage is that the maximum output power may not be realized due to a few design constraints. Given the advantages of the scalable models adopted in the study, the design parameters of the diesel engines and motors are selected as the optimization variables. In addition to the design parameters, the parameters used in the energy management strategy, such as the available boundary of the battery, are determined as significant in the optimal design for hybrid electric ships [33]. Overall, five design parameters and two energy management parameters are selected as the

(a) Battery driving mode   (b) Genset driving mode   (c) Battery charging mode
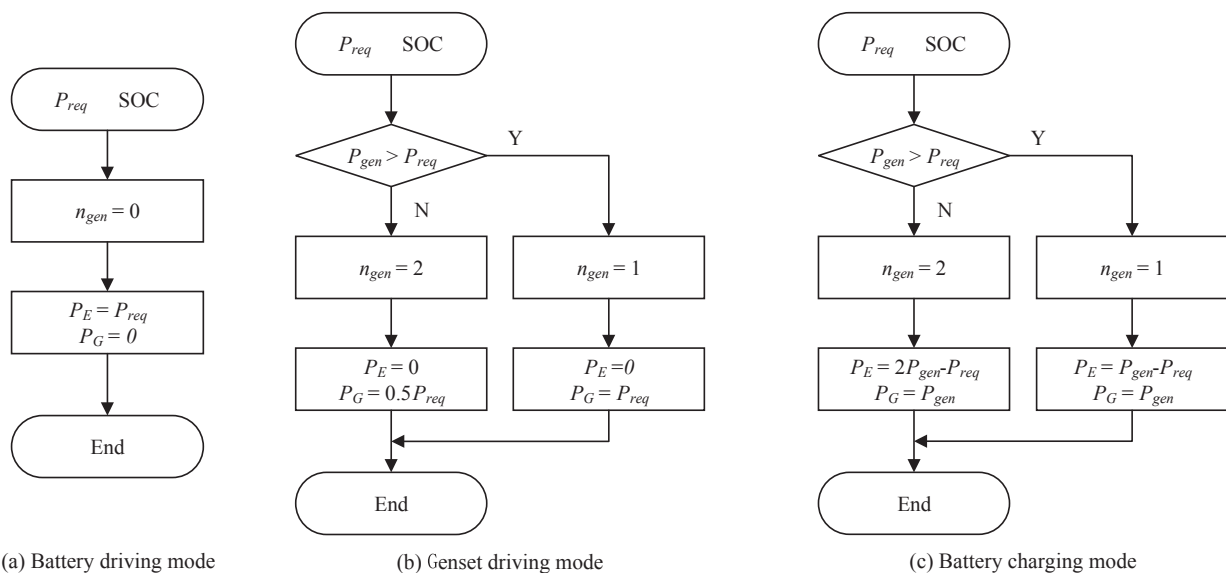
Fig. 3. Energy management strategy in the three modes.

optimization variables in the study. The five design parameters include the displacement V_d of each diesel engine, diameter d_m and length l_m of each motor rotor, gear ratio i, and number n_{ser} of the battery modules in series. The two energy management parameters include B_{up} and B_{low}, which correspond to the upper and lower bounds of the battery SOC.

4.2. Objective function

The optimization problem considers three optimization indexes, namely fuel consumption, GHG emission, and lifecycle cost. The objective involves minimizing the three indexes. Thus, the multi-objective functions are expressed as follows:

$$\begin{cases} \min\{f_1, f_2, f_3\} \\ f_1 = m_{year} \\ f_2 = GHG_{year} \\ f_3 = C_{life} \end{cases} \tag{36}$$

The calculation of annual fuel consumption (m_{year}), annual GHG emission (GHG_{year}) and lifecycle cost (C_{life}) are described in detail in the following subsections.

4.2.1. Fuel consumption
The annual fuel consumption of the HEPS is expressed as follows:

$$m_{year} = \int \dot{m}_f \, dt \tag{37}$$

4.2.2. GHG emission
The annual GHG emission of the HEPS is divided into two parts, namely which are produced by fuel and electricity, respectively [34]:

$$GHG_{year} = C_{fuel} m_{year} + I_{ele} E_{chr} \tag{38}$$

where C_{fuel} denotes the average GHG emission factor of fuel during the lifecycle; E_{chr} denotes the accumulated electricity from the shore power plant charged into the battery of the HEPS; and I_{ele} denotes the average GHG intensity of the electricity transmitted from the shore power plant. In several countries including China, nearly 75% of electricity is produced by coal, and the average coal consumption is 0.33kg/kW·h [35]. Thus, the value of I_{ele} is approximately 0.85 kg/kW·h [34].

The GHG emission from the consumed fuel is further classified into two parts, namely the well-to-tank (WTT) part and tank-to-propeller (TTP) part. The GHG emission of the WTT part is due to crude extraction and processing, crude transport, fuel refining, and fuel distribution and dispensing. The GHG emission of the TTP part is due to the combustion of the diesel engine. As a whole, the calculation of the GHG emission factor C_{fuel} is summarized in the following formula [14]:

$$C_{fuel} = C_{fuel-WTT} \cdot L_{CV} \cdot 10^{-9} + C_{fuel-TTP} \tag{39}$$

where $C_{fuel-WTT}$ denotes the factor of the WTT part, L_{CV} denotes the lower calorific value, and $C_{fuel-TTP}$ denotes the factor of the TTP part. For the common diesel oil used in ships, the value of $C_{fuel-WTT}$, L_{CV}, and $C_{fuel-TTP}$ are 1.42×10^{-5} g/J, 4.27×10^4; J/g, and 3.17, respectively [36,37].

Thus, the GHG emission intensity of fuel is 0.31 kg/kW·h and is calculated as follows:

$$I_{fuel} = C_{kWhJ} \cdot C_{fuel} / L_{CV} \tag{40}$$

where C_{kWhJ} denotes the unit conversion factor from kW·h to J (3.6×10^6 J/kW·h), and L_{CV} denotes the lower calorific value that equals to 4.27×10^7 J/kg for the fuel used in marine diesel engines.

4.2.3. Lifecycle cost
In addition to the initial investment and operational cost, the lifecycle cost of the HEPS should certainly include the cost of the battery replacement. By using the net present values, the total lifecycle cost is calculated as follows:

$$C_{life} = C_{ini} + C_{bat} + C_{ope} \tag{41}$$

where C_{inc}, C_{bat}, and C_{ope} denote the initial investment, cost of battery installation, and operational cost, respectively.

With respect to the initial investment, the three types of components, namely the diesel engines, generators, and motors are the costliest. Therefore, the initial investment are estimated by the following formula [34]:

$$C_{ini} = 2c_{main} P_{main} + 2c_{gen} P_{gen}(1 + 0.06) + 2c_{motor} P_{motor} \tag{42}$$

where c_{main}, c_{gen}, and c_{motor} denote the unit cost of the diesel engine, generator, and motor, respectively; P_{main}, P_{gen}, and P_{motor} denote the rated power of diesel engine, generator, and motor, respectively.

Generally, the battery should be replaced several times during the lifecycle of the AHTS vessel. Furthermore, an inflation rate exists. Hence, the accumulated cost of the battery is calculated as follows [38].

$$C_{bat} = \sum_{i=1}^{N_{rep-bat}} c_{i-bat} \left(\frac{1 + g_{bat}}{1 + I_a} \right)^{i \cdot T_{life}} \tag{43}$$

where $N_{rep-bat}$ denotes the total number of battery replacements during the lifetime (Y), g_{bat} denotes the annual inflation rate, I_a denotes the annual interest rate, and T_{life} denotes the lifetime of lithium-ion battery. The calculation of the initial investment of each new battery as denoted by c_{i-bat} is given as follows:

$$c_{i-bat} = c_{bat} Q_{bat} \tag{44}$$

where c_{bat} denotes the unit price of the lithium-ion battery.

The calculation of $N_{rep-bat}$ is given as follows [38]:

$$N_{rep-bat} = \text{int}\left[\frac{Y}{T_{life}} \right] \tag{45}$$

Operational cost occurs every year during the lifetime. The operational cost C_{ope} is calculated as follows [38].

$$C_{ope} = \sum_{i=1}^{Y} c_{ope} \left(\frac{1 + g_{ope}}{1 + I_a} \right)^i \tag{46}$$

where c_{ope} denotes the operational cost each year, and g_{ope} denotes the annual inflation rate in terms of the operational cost.

The yearly operational cost accounts for the fuel fed to the diesel engines and the electricity charged from the shore power plant to the battery. The calculation is given as follows [34].

$$c_{ope} = c_{fuel} m_{year} + c_{ele} E_{chr} \tag{47}$$

where c_{fuel} and c_{ele} denote the unit cost of the fuel and electricity from the shore power, respectively.

4.3. Constraints

It is necessary for the design of the HEPS to satisfy the following conditions that correspond to the constraints of the optimization problem.

$$v_{max} \leqslant v_{req} \tag{48}$$

$$P_{req-max} \leqslant 2P_{gen} \tag{49}$$

$$num_{battery} \leqslant num_{max} \tag{50}$$

$$10\% \leqslant SOC \leqslant 90\% \tag{51}$$

The constraints are explained as follows.

(1). With respect to the safety consideration, the maximum velocity v_{max} of the design of the AHTS should be less than the limitation v_{req}.
(2). In order to fulfil the voyage task, the total rated output power $2P_{gen}$ of the generators (two generators are used in the HEPS) should

exceed the maximum required power of the AHTS.

(3). With respect to the installation space consideration, the number n_{ser} of the battery modules should be less than the limitation num_{max}.

(4). With respect to the battery health consideration, the available SOC ranges from 10% to 90% [39,40].

4.4. Optimization algorithm

The optimal design of the HEPS is formulated as a constrained nonlinear multi-objective optimization problem, and thus the NSGA-II algorithm is incorporated into design space exploration. The NSGA-II method is a type of multi-objective evolutionary algorithm that evolved from the genetic algorithm that inspired Darwin's concept of natural selection in which three genetic operators including "selection", "crossover", and "mutation" act collectively to ensure the optimization [41,42]. Specifically, "selection" weeds out unfit designs; "crossover" ensures that the characteristics of the parent population can be transferred to the next generation; and "mutation" helps in avoiding trapping in the local optimum. Therefore the NSGA-II exhibits advantages in solving highly nonlinear problem and is used in the design of hybrid power generator systems [42].

In a manner different from classical genetic algorithms, the NSGA-II introduces the fast non-dominated sorting operator and crowded comparison operator to implement the multi-objective searching and increase the computation speed [21]. Based on the fast non-dominated sorting operator, solutions in the first non-dominated front are labeled as domination count zero ($n_p = 0$), and the domination count n_p can be at most one less than the number of populations ($N - 1$). The crowded comparison operator assesses the density of solutions surrounding an individual and is introduced to evaluate individuals with the same domination count, and the individual located in a lesser crowded area dominates.

The implementation flowchart of the NSGA-II is shown in Fig. 4. At the initialization stage, the design parameters of the initial parent population are randomly generated. Subsequently, the offspring of the parent population is produced using the methods of "selection", "crossover", and "mutation". Thus, the parent and offspring population constitute the first population group. Each individual in the group calls the HEPS model functions once, and this returns the optimization indexes (fuel consumption m_{year}, GHG emission GHG_{year} and cost C_{life}). By applying the criterion of fast non-dominated sorting and crowding distance comparison, a few individuals are selected to constitute the new parent population. This iteration continues until the number of iterations reaches the maximum limit, and the NSGA-II can produce a quantity of design solutions. By using the method of fast non-dominated sorting, a few of the solutions are selected to form the Pareto solution set.

5. Results and discussion

In this section, the operating profile of the AHTS vessel is defined by considering both the propulsive and non-propulsive loads. Following this, the Pareto solution sets calculated from the NSGA-II algorithm and MOPSO algorithm are compared. Thereafter, the optimal design is selected from the solution sets. In order to evaluate the performance of the optimal design, a real-time HIL experimental platform is constructed. Subsequently, performance tests are conducted on the platform. The results of the multi-objective NSGA-II are compared with those from a single objective genetic algorithm and also with those from a conventional benchmark vessel.

5.1. Operating profile

In the absence of a standardized operation cycle for AHTS vessels, a velocity profile of a tug boat collected from real operation data is adopted in the study by referring to extant studies [43] as shown in Fig. 5(a). The velocity profile includes two types, namely the cruising
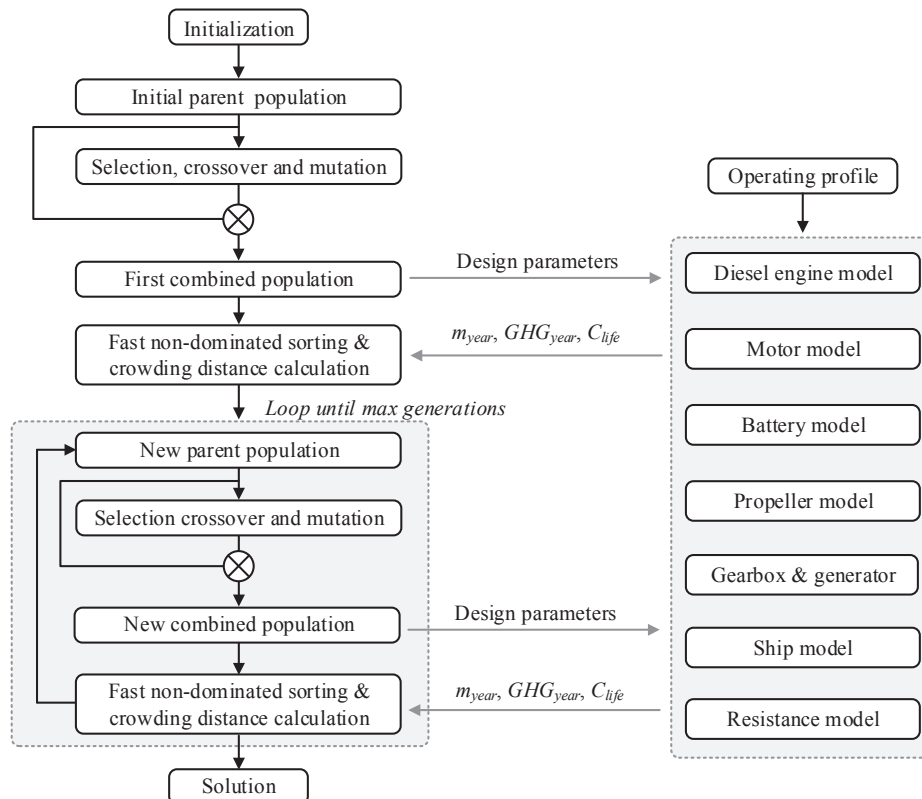
Fig. 4. Scheme of the NSGA-II and its interaction with mathematical models.

(a) Velocity profile

(b) Propulsive load profile

(c) Non-propulsive load profile
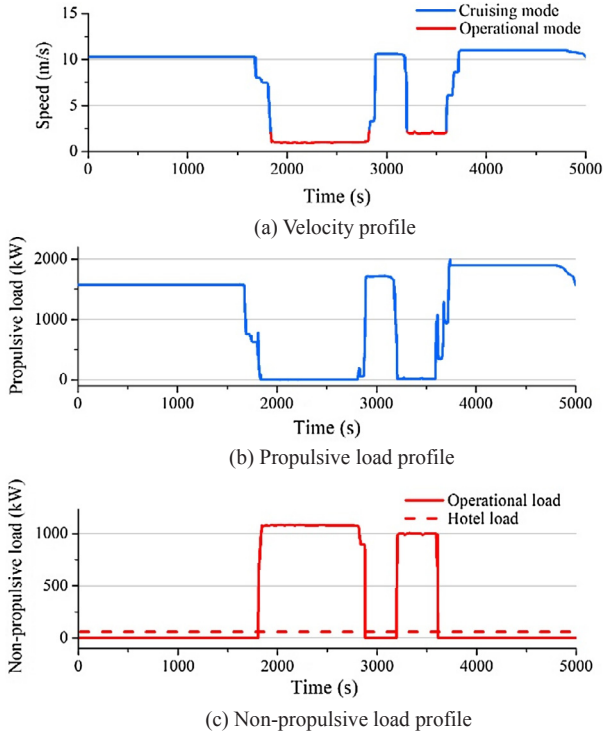
Fig. 5. Operating profile of the examined AHTS vessel [43]

mode and operational mode. In the cruising mode, the AHTS vessel sails at a high speed for most of the time to reach the operating site quickly. Conversely, in the operational mode, the AHTS vessel sails at a low speed and performs operations such as lifting and pulling. Thus, the propulsive load profile is calculated from the velocity profile and is shown in Fig. 5(b). In addition to the propulsive load, it is not possible to ignore the non-propulsive load that consists of the operational load and hotel load for the AHTS vessel. Given the demanded power of cranes and capstans, the operational load and hotel load are estimated as shown in Fig. 5(c). The duration of the profiles plotted in Fig. 5 is 5000 s. The AHTS vessel is assumed to run 6 times a day and 200 days per year. As mentioned in the subsection on energy management strategy, shore power is available to charge the battery after each one-day-voyage.

5.2. Pareto solution set

The Pareto solution set obtained by the NSGA- II is plotted in Fig. 6 given the range of the optimization variables shown in Table 2. The MOPSO is also a popularly used multi-objective optimization method,
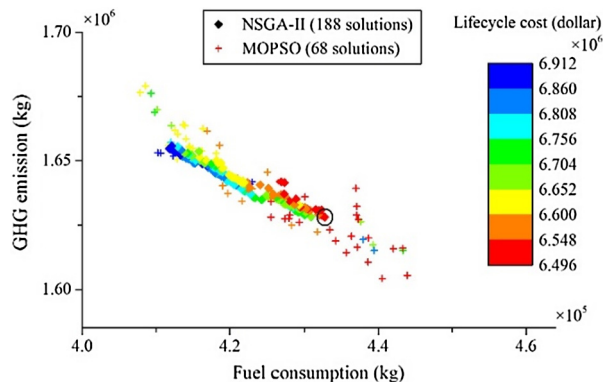
Fig. 6. Pareto solution sets obtained by NSGA-II and MOPSO.

Table 2
Range of the optimization variables and optimal solutions.

Optimization variable	Range	NSGA-II (close to MOPSO)	SOGA
Displacement of the diesel engine V_d (10^{-3}m³)	[80 130]	71.00	123.15
Diameter of the motor rotor d_m (m)	[0.30 0.90]	0.54	0.59
Length of the motor rotor l_m (m)	[0.30 0.90]	0.50	0.39
Gear ratio i	[10 20]	14.14	18.45
Number of the battery module in series n_{ser}	[55 235]	84	234
Lower bound of SOC B_{low} (%) B_{low}	[10.00 30.00]	18.23	11.22
Upper bound of SOC B_{up} (%)	[70.00 90.00]	77.08	85.08

and thus the Pareto solution set obtained by the MOPSO is also provided for comparison purposes. As shown in Fig. 6, the two solution sets appear to be similar, and this validates the accuracy of the implementation of the two optimization methods.

Conversely, the difference between the two solution sets is determined by the analysis in detail. First, the number of solutions is different. There are 188 solutions in the Pareto solution set by the NSGA- II in contrast to 68 by the MOPSO. Thus, the NSGA- II determines more effective solutions to form the Pareto solution set. Second, the distribution of the solutions is different. The quality of the Pareto set can be evaluated by the criteria of spacing metric [44]. With respect to the three optimization indexes described in the Pareto solution set, the spacing metric that is represented by s is calculated using the following equations:

$$d_i = \min_j (|f_1^i(\mathbf{x}) - f_1^j(\mathbf{x})| + |f_2^i(\mathbf{x}) - f_2^j(\mathbf{x})| + |f_3^i(\mathbf{x}) - f_3^j(\mathbf{x})|)j$$
$$= 1, 2, ..., n; i \neq j \tag{52}$$

$$s = \left[\frac{1}{n-1} \sum_{i=1}^{n} \left(\frac{d_{ave} - d_i}{d_{ave}} \right)^2 \right]^{\frac{1}{2}} \tag{53}$$

where d_{ave} denotes the mean value of all d_i, and n denotes the number of Pareto solutions. The spacing metric s can aid in recognizing the monotonous dispersion of solution in the Pareto chart. A decrease in the spacing metric s results in a more optimal solution because the solutions are more uniformly distributed. The spacing metric s of the Pareto solution set from the NSGA- II is 1.77 while that from the MOPSO is 1.88. Thus, the NSGA- II results in a slightly more optimal Pareto solution set when compared to that in the MOPSO.

As widely-known, each solution of the Pareto solution set is optimal although it is generally impossible for any one of the three optimization indexes to simultaneously reach the minimum for a multi-objective optimization problem. The study emphasizes on GHG emission and cost by introducing them into the optimization objective. Hence, a solution with relative low GHG emission and relative low cost denoted in black in Fig. 6, is selected as the objective solution that is tested on the experimental platform. The values of the optimization variables of the solution are listed in Table 2. The results indicate that the selected solution is obtained by the NSGA- II, and it is close to a solution by the MOPSO. Thus, it is unnecessary to present the results of the solution determined by the MOPSO due to its similarity.

5.3. Hardware-in-the-loop experimental platform

A HIL experiment is performed to evaluate the performance of the optimal designs for HEPSs. The experimental platform consists of a real-time energy management platform and a real-time driveline model platform. Both are software-hardware development platforms based on MATLAB/Simulink that rapidly generate the code in C language and
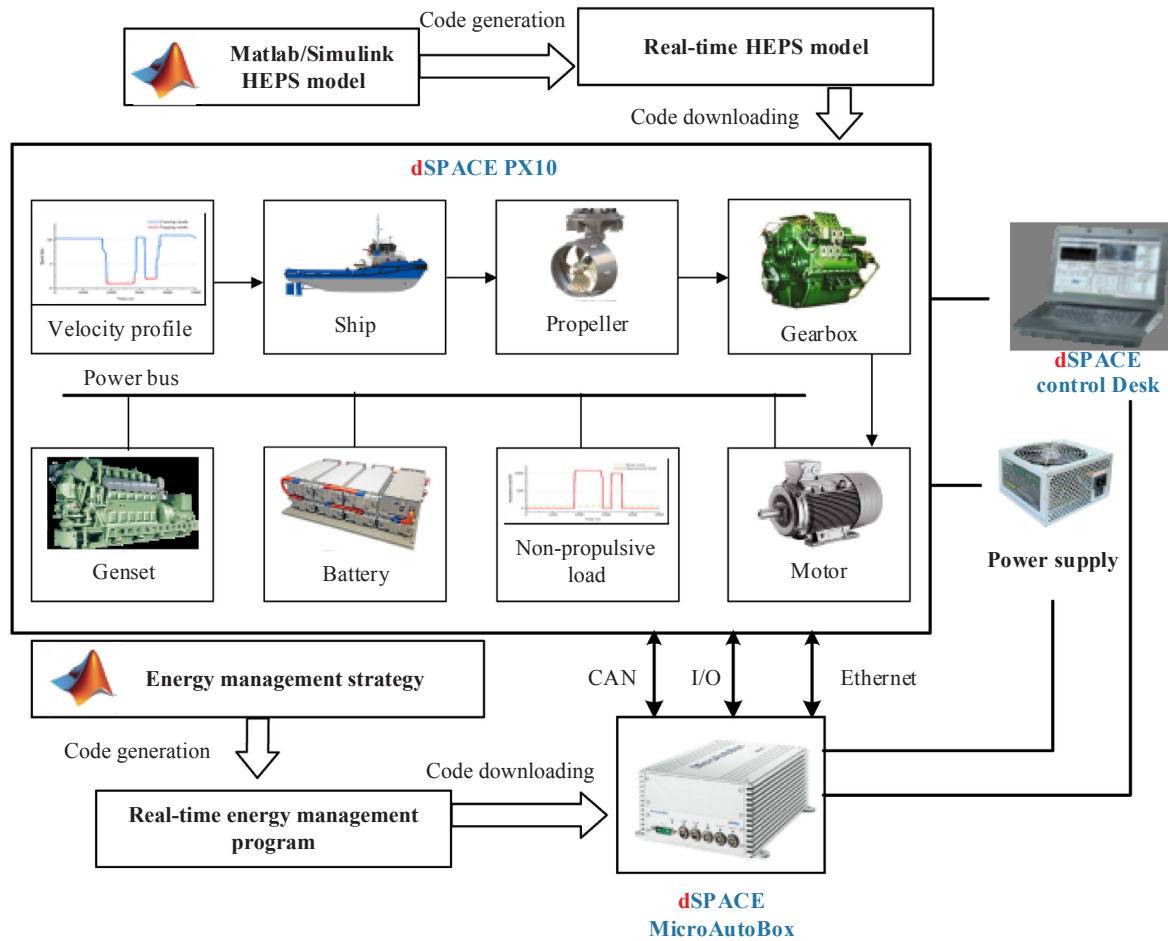
Fig. 7. Schematic diagram of the HIL experimental platform.

perform online calibration.

The development process of the HIL experimental platform consists of three steps. First, the driveline models and energy management strategy are constructed in the MATLAB environment. Second, the real-time kernel of the driveline models is generated by MATLAB/Simulink automatic code generation technology and the real-time kernel of the energy management strategy. Third, the dSPACE software tool that is termed as ControlDesk downloads the real-time kernel of the driveline models into the dSPACE hardware PX10 that exhibits high real-time computing capacity. Additionally, the kernel of the energy management strategy is downloaded into the MicroAutobox that is an electronic controller hardware. The scheme of the real-time experimental platform is shown in Fig. 7. The variables in PX10 and MicroAutobox are monitored and calibrated through ControlDesk running on a desktop.

The input and output signals of the HEPS HIL experimental platform are shown in Fig. 7. The CAN and I/O interfaces are used for the communication between PX10 and MicroAutobox. The communication with ControlDesk is through the interface of Ethernet. A photo of the HIL experimental platform is shown in Fig. 8.

5.4. Experimental results

The driveline of a conventional tug vessel is considered as the benchmark of the examined HEPS. The parameters of the tug vessel are listed in A. Table 1 of Appendix. The results of the conventional propulsive system are represented by "Conv.". With respect to the optimal design of the HEPS, in addition to the proposed NSGA-II, a single-objective genetic algorithm (SOGA) that pursues only fuel consumption is also implemented for comparison purposes. The values of the
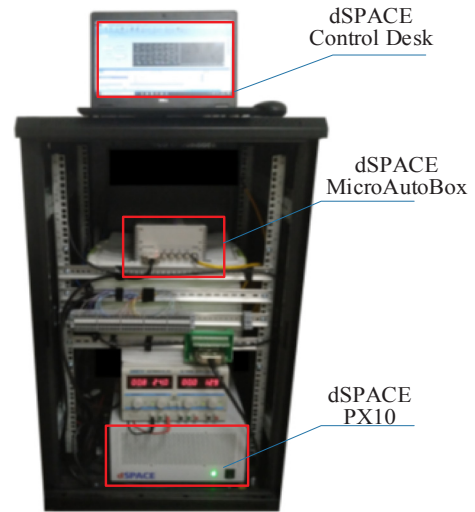
Fig. 8. HIL experimental platform.

optimization variables of the solution obtained by the SOGA are provided in the last column of Table 2. The performance of the NSGA-II designed HEPS, SOGA designed HEPS, and the conventional propulsive system are compared in terms of the three indexes, i.e., fuel consumption, GHG emission, and lifecycle cost. The maps of the baseline diesel engine and motor are plotted in A. Figs. A1 and A. A2, respectively. Other simulation parameters are listed in A. Table A2 .

As shown in Fig. 9(a), the fuel consumptions resulting from the
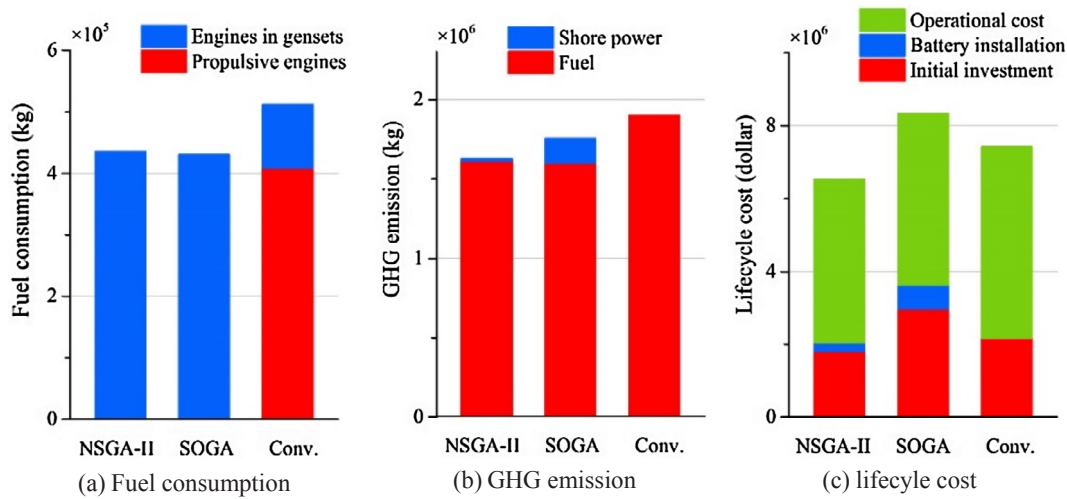
Fig. 9. Comparison of the optimization indexes.
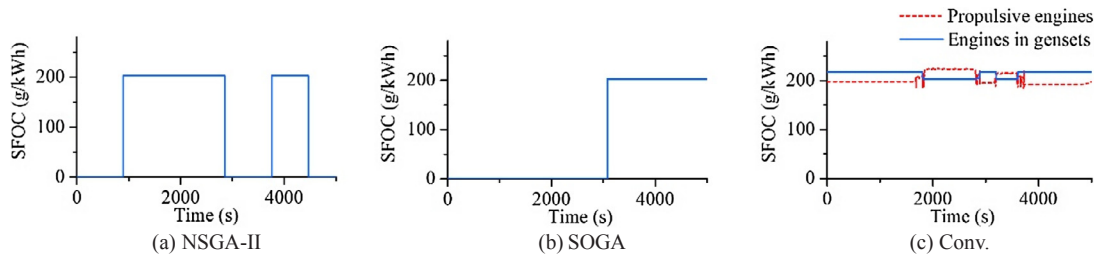
Fig. 10. Comparison of specific fuel consumption.

NSGA-II, SOGA, and conventional propulsive system are 4.35×10^5 kg, 4.4×10^5 kg and 5.12×10^5 kg, respectively. Therefore, the HEPS designed by both the NSGA-II and SOGA achieves less fuel consumption than that of the conventional propulsive system. Specifically, the NSGA-II reduces by 14.99%, and the SOGA reduces by 15.85%.

As shown in Fig. 9(b), the GHG emissions accumulated for a year from the NSGA-II, SOGA, and conventional propulsive system are 1.63×10^6 kg, 1.75×10^6 kg and 1.90×10^6 kg, respectively. Therefore, the HEPS, designed by both the NSGA-II and SOGA achieves less GHG emission when compared to that of the conventional driveline. Specifically, the NSGA-II reduces by 14.12%, and the SOGA reduces by 7.75%.

As shown in Fig. 9(c), the total lifecycle costs resulting from the NSGA-II, SOGA, and conventional propulsive system are "$"$6.52 \times 10^6$, "$"8.34×10^6 and "$"$7.42 \times 10^6$, respectively. The HEPS is different from the other two performance indexes since it can be cheaper or more expensive than the conventional propulsive system. Specifically, the NSGA-II can reduce the lifecycle cost by 12.11% while the SOGA increases by 12.31%.

In summary, the HEPS obtained by the NSGA-II achieves three better performance indexes when compared with that of the conventional driveline while the HEPS by the SOGA achieves two higher performance indexes (fuel consumption and GHG emission) and an inferior index (cost). These results are essentially in agreement with other studies on HEPSs with respect to the advantages of fuel saving and emission reduction.

Nevertheless, a comparison between the results of the NSGA-II and SOGA should be more interesting. The fuel consumption obtained by the NSGA-II is 1.05% higher that by the SOGA. However, the GHG emission of the former is 7.34% less than the latter. Furthermore, the lifecycle cost of the former is 21.75% less than the latter. Thus, the NSGA-II designed HEPS achieves significant improvement in emission and cost by sacrificing fuel consumption. It is observed that the increase

in the percentage of fuel consumption is significantly less than the decrease in the percentage of the emission and lifecycle cost. Hence, the tradeoff between fuel consumption and emission/cost gives expression to the advantage of the NSGA-II, a multi-objective optimization.

The insights of the optimal designs are analyzed in the next subsection.

5.5. Discussion

The amount of the fuel consumption is determined by the working time and specific fuel oil consumption (SFOC) of the engines. In a 5000 s voyage, the engine working time of the NSGA-II design is 2668 s and exceeds that of the SOGA design (1917 s) although it is significantly lower than that of the conventional propulsive system (5000 s) as shown in Fig. 10. All gensets of the NSGA-II design rest collectively for 2332 s. Similarly, all gensets of the SOGA design rest collectively for 3083 s as shown in Fig. 11. Hence, the engines of the HEPS, designed by either the NSGA-II or SOGA can rest and do not consume fuel for some time although the engines of the conventional propulsive system work and consume fuel throughout. It is observed that the engine is restarted four times for the NSGA-II design, twice for the SOGA design, and twice for the conventional propulsive system. Although the restart operation of the engine typically leads to high SFOC, the total fuel consumption is not significantly affected because the restart process is short, and the number of restart times is very low. The NSGA-II and SOGA obtains the SFOC as low as 203 g/kW·h during the engine working time that can be maintained by using the electric energy to/from the battery of the HEPS. When the demanded load power is low, the engines of the conventional propulsive system must work in the low efficiency area, and thus the engine SFOC increases up to 225 g/kW·h, which is 11.0% higher than the SFOC of the engines in the HEPS. However, when the demanded load power is relatively high such that engines can work in a high efficiency area, the engine SFOC can reach 197 g/kW·h that is 3.0%
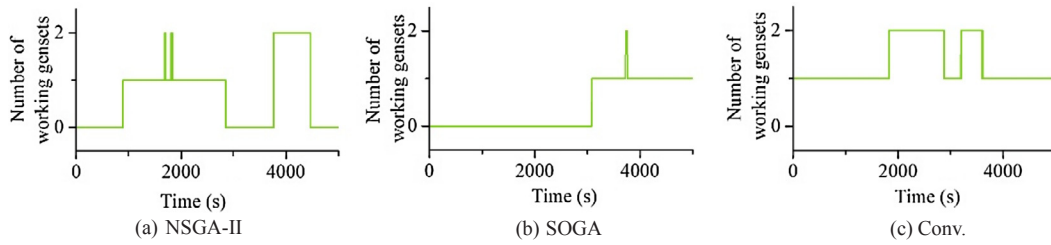
Fig. 11. Comparison of the genset schedule.

(a) Battery SOC variation   (b) Battery power variation   (c) Shore power consumption
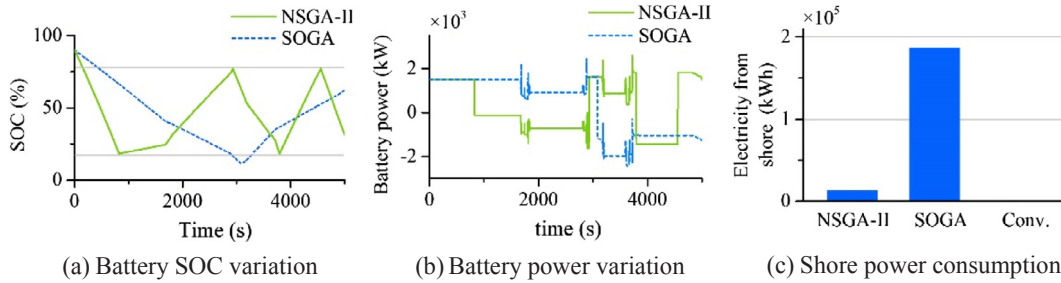
Fig. 12. Comparison of the battery usage.
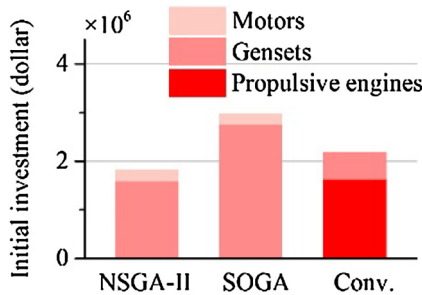
Fig. 13. Comparison of initial investment (not incl. battery).

lower than the SFOC of the engines in the HEPS. This is because the direct mechanical link from the engines to the propellers reduces conversion loss between mechanical and electrical energy flow. Overall, the fuel consumption of the HEPS designed by the NSGA-II exceeds that by the SOGA due to the longer working time of the engines. Conversely, the fuel consumption of the HEPS designed by the NSGA-II is less than that of the conventional propulsive system due to the shorter working time of the engines and lower SFOC in the case of low load power.

In addition to the power supplied by the diesel engines, the electric power supplied by the shore plant plays an important role in the HEPS. Therefore, the GHG emission should consider the consumed fuel as well as the consumed electricity. The electricity supplied by the shore plant is charged into the battery. The battery SOC changes between 10% and 90% in a 5000-s voyage as shown in Fig. 12(a). The data in Table 1 suggests that the battery size of the NSGA-II design is approximately one third of the SOGA design. Therefore, the battery power capacity of the NSGA-II design is less than that of the SOGA design as shown in Fig. 12(b). We recall the energy management strategy in which a battery is charged to the upper SOC bound daily before the vessel begins its one-day-voyage, and the electricity charged from the shore power plant of the NSGA-II design is less than that of the SOGA design as shown in Fig. 12(c). It is observed that the GHG emission intensity of electricity that is produced by coal is significantly higher than that of fuel. As expressed in the subsection on GHG emission modeling, the average GHG emission intensity of electricity is 0.85 kg/kW·h. Conversely, the GHG emission intensity of fuel is 0.31 kg/kW·h.

Thus, the NSGA-II design consumes 1.2×10^4 kW·h electricity from the shore power plant as shown in Fig. 12(c) and correspondingly

produces 1.0×10^4 kg GHG emission from the electricity as shown in Fig. 9(b). Conversely, the SOGA design consumes 1.9×10^5 kW·h electricity from the shore power plant and produces 1.5×10^5 kg GHG emission from the electricity. Hence, the data of the NSGA-II design is less than one tenth of the data of the SOGA design. Thus, the total GHG emission reduction of the NSGA-II design is due to the low amount of electricity from the shore plan, that can even compensate the increased fuel consumption to a certain extent. In contrast, the total GHG emission of the SOGA design increases due to the high amount of electricity from the shore plant although the fuel consumption is reduced.

A significant finding is that the NSGA-II design costs the least among the three designs shown in Fig. 9(c). The composition of the initial investment is shown in Fig. 13. When compared with the conventional propulsive system, the NSGA-II design reduces the cost in terms of two aspects. The first involves reducing the initial investment from "$"$2.2 \times 10^6$ to "$"$1.8 \times 10^6$, and this is mainly due to less usage of two engines. The second involves reducing the operational cost from "$"$5.2 \times 10^6$ to "$"$4.5 \times 10^6$, and this is mainly due to the decrease in fuel consumption. Conversely, when compared with the SOGA design, the NSGA-II design achieves lower cost in two different aspects. The first involves reducing the battery cost from "$"$6.6 \times 10^5$ to "$"$2.4 \times 10^5$ by using a smaller sized battery. The second involves reducing the initial investment from "$"$3.0 \times 10^5$ to "$"$2.4 \times 10^5$ by using smaller engines.

From the above, the application of the NSGA-II method in the study determines an optimal design that significantly reduces the GHG emission and lifecycle cost by sacrificing low fuel consumption. In the case in which the single objective optimization outcomes designs with low fuel consumption result in high GHG emission and high cost, the multi-objective optimization is of immense significance in the design of HEPSs and especially in those areas where electricity is mainly produced by coal. The effectiveness of the proposed NSGA-II method is validated by the application of the examined AHTS vessel.

5.6. Future research directions

The multi-objective optimization method is applied to the design of various HEPSs such as offshore vessels and scientific research vessels. Different HEPS architectures are subject to different constraints for the optimization, and thus different solution sets can be explored. Evidently, the method can also be extended to hybrid electric vehicles. Specifically, the method can explore better solutions for plug-in hybrid

electric vehicles that use electricity from grids.

The examined multi-objective optimization method can be improved in terms of at least three aspects: (1) upgrading the rule-based energy management strategy to an advanced optimal management strategy; (2) developing bilayer optimization by integrating the optimal sizing and optimal energy management into a comprehensive optimal package; and (3) introducing more accurate transient models of fuel consumption and emission that address the effect of stop-and-go operation.

6. Conclusion

The present study focuses on the problem wherein electricity from shore plants reduces fuel consumption while significantly increasing GHG emissions in areas where electricity is mainly produced from coal. Hence, a multi-objective optimization for the design of a hybrid diesel/battery/shore power propulsive system was proposed by considering fuel consumption, GHG emission, and lifecycle cost. The NSGA-II method was developed to explore an optimal design. In addition to the modeling and simulation of the examined HEPS vessel, a real-time HIL experimental platform was constructed to validate the effectiveness of the optimization. The test results indicated that the NSGA-II finds the optimal design resulting in 7.34% less GHG emission and 21.75% less lifecycle cost at the expense of a 1.03% increase in fuel consumption, when compared with the single objective optimization that pursues only minimum fuel consumption. Furthermore, when compared with the conventional propulsive system, the NSGA-II exhibits advantages in all the three aspects, i.e., 14.99% less fuel consumption, 14.12% less GHG emission, and 12.11% less lifecycle cost. With respect to environmental protection, multi-objective optimization is of importance in the design of HEPSs, especially in those areas where electricity is mainly produced using coal. The proposed multi-objective optimization method can be applied to the design of various HEPSs such as offshore vessels, research and exploration vessels.

Appendix A

Tables A.1 and A.2,Figs. A1 and A2.

Table A.1
Specification of the benchmark vessel [45].

Parameter	Value
Length (over all) (m)	66.00
Breadth (m)	16.00
Depth (m)	7.30
Draught (m)	6.20
Propulsive engine (kW) (AMG55 by MAN)	3285×2
Genset (kW) (LG975MN, D2862LE223 by MAN)	720×2
Pulling capacity (kg)	1.2×10^5

Table A.2
Parameters used in the simulation.

Parameter	Nomenclature	Value
$B_{base}(m)$	Bore of the baseline engine	0.128
c_{11}	After-body shape factor	1.03
c_{12}	Draught factor	0.59
c_{bat} ("$/kWh)	Unit cost of a lithium-ion battery	175
c_{ele} ("$/kWh)	Unit cost of shore power	0.08
c_{fuel} ("$/ton)	Unit cost of diesel fuel	520
c_{gen} ("$/kW)	Unit cost of a genset	350
c_{main} ("$/kW)	Unit cost of the main engine	250
c_{motor} ("$/kW)	Unit cost of the motor	32
C_B	Bulbous bow resistance coefficient	0
C_F	Resistance coefficient of frictional resistance	1.87×10^{-3}
ΔC_F	Compensation for C_F	0.40×10^{-3}
C_{BTT}	Appendage resistance of the bow thruster tunnel coefficient	4.04×10^{-3}
C_P	Prismatic coefficient	0.5833
C_{TS}	Additional pressure resistance coefficient	0
C_W	Wave-making and wave-breaking resistance coefficient	1.87×10^{-3}
$d(m)$	Draught of the vessel	6.2
$d_m(m)$	Diameter of the rotor of baseline motor	0.6416
$D(m)$	Propeller diameter	3.8
g_{bat}	Annual inflation rate of the battery price	3%
g_{ope}	Annual inflation rate of the operational cost	3%
I_a	Annual interest rate	5%
K_{Q1}	Torque factor 1	−0.0186

(*continued on next page*)

Table A.2 (*continued*)

Parameter	Nomenclature	Value
K_{Q2}	Torque factor 2	−0.0399
K_{Q3}	Torque factor 3	0.0680
K_{T1}	Thrust factor 1	−0.1060
K_{T2}	Thrust factor 2	−0.3246
K_{T3}	Thrust factor 3	0.45946
$l_m(m)$	Length of the rotor of the baseline motor	0.3343
l_{cb}	Longitudinal position of the buoyant center	−0.75%
$L_R(m)$	Length coefficient	26.20
$m(kg)$	Mass of the vessel	1.7×10^6
num_{max}	Maximum number of battery modules	250
N_p	Number of propeller	2
$S(m^2)$	Wet-surface area of the hull	1347.12
$S_{APP}(m^2)$	Appendage wetted area	81.02
$S_{base}(m)$	Stroke of baseline engine	0.157
$T_{life}(year)$	Lifetime of lithium-ion battery	5
$v_{req}(m/s)$	Required maximum speed	7.71
$Y(year)$	Lifetime of the HEPS	25
η_{gear}	Efficiency of the gearbox	0.98
η_{gen}	Efficiency of the generator	0.97
$\rho(kg/m^3)$	Density of sea water	1.025×10^3
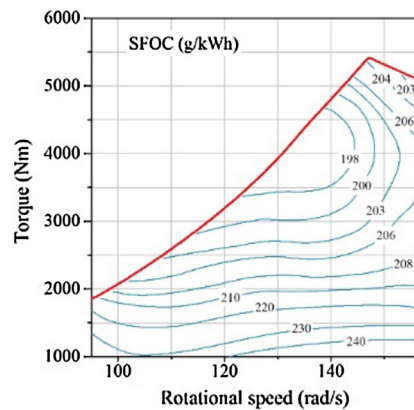
Fig. A1. SFOC map of the baseline diesel engine [46].
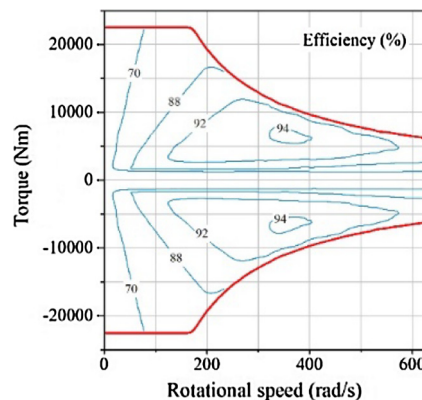
Fig. A2. Efficiency map of the baseline motor [34].

References

[1] Mccarthy JH. On the calculation of thrust and torque fluctuations of propellers in nonuniform wake flow. Sens Actuators, B 1961;161:80–7.

[2] Geertsma RD, Negenborn RR, Visser K, Hopman JJ. Design and control of hybrid power and propulsion systems for smart ships: a review of developments. Appl Energy 2017:30–54.

[3] Veneri, Migliardini, Capasso, Corbo. Overview of electric propulsion and generation architectures for naval applications. IEEE Electrical Systems for Aircraft, Railway and Ship Propulsion (ESARS), Bologna, Italy; 2012. p. 1–6.

[4] Hou J, Sun J, Hofmann HF. Mitigating power fluctuations in electric ship propulsion

with hybrid energy storage system: design and analysis. IEEE J. Oceanic Eng 2017:1–15.

[5] Díaz-De-Baldasano MC, Mateos FJ, Núñez-Rivas LR, Leo TJ. Conceptual design of offshore platform supply vessel based on hybrid diesel generator-fuel cell power plant. Appl Energy 2014;116:91–100.

[6] Baldi F, Ahlgren F, Melino F, Gabrielii C, Andersson K. Optimal load allocation of complex ship power plants. Energy Convers Manage 2016;124:344–56.

[7] Hansen JF, Wendt F. History and state of the art in commercial electric ship propulsion, integrated power systems, and future trends. Proc IEEE 2015;103:1–14.

[8] De Breucker S, Driesen J, Peeters E. Possible applications of plug-in hybrid electric ships. IEEE Electric Ship Technologies Symposium; 2009. p. 310–7.

[9] Lan H, Wen S, Hong YY, Yu DC, Zhang L. Optimal sizing of hybrid PV/diesel/battery in ship power system. Appl Energy 2015;158:26–34.

[10] Vu TL, Ayu AA, Dhupia JS, Kennedy L. Power management for electric tugboats through operating load estimation. IEEE Trans Control Syst Technol 2015;23:2375–82.

[11] Lee KJ, Shin D, Yoo DW, Choi HK, Kim HJ. Hybrid photovoltaic/diesel green ship operating in standalone and grid-connected mode – Experimental investigation. Energy 2013;49:475–83.

[12] Skinner BA, Parks GT, Palmer PR. Comparison of submarine drive topologies using multiobjective genetic algorithms. Vehicular Technol IEEE Trans 2009;58:57–68.

[13] Soleymani M, Yoosofi A, Kandi-D M. Sizing and energy management of a medium hybrid electric boat. J Mar Sci Technol 2015;20:739–51.

[14] Ribau JP, Silva CM, Sousa JMC. Efficiency, cost and life cycle CO2 optimization of fuel cell hybrid and plug-in hybrid urban buses. Appl Energy 2014;129:320–35.

[15] Völker T. Hybrid propulsion concepts on ships. 33rd International Scientific Conference. Science in Practice; 2013. p. 66–76.

[16] Hui S. Multi-objective optimization for hydraulic hybrid vehicle based on adaptive simulated annealing genetic algorithm. Eng Appl Artif Intell 2010;23:27–33.

[17] Mora AM, Merelo JJ, Castillo PA, Arenas MG. HCHAC: a family of MOACO algorithms for the resolution of the bi-criteria military unit pathfinding problem. Comput Oper Res 2013;40:1524–51.

[18] Borhanazad H, Mekhilef S, Ganapathy VG, Modiri-Delshad M, Mirtaheri A. Optimization of micro-grid system using MOPSO. Renew Energy 2014;71:295–306.

[19] Ahmadi P, Dincer I, Rosen MA. Multi-objective optimization of a novel solar-based multigeneration energy system. Sol Energy 2014;108:576–91.

[20] Ghodratnama A, Jolai F, Tavakkoli-Moghaddam R. Solving a new multi-objective multi-route flexible flow line problem by multi-objective particle swarm optimization and NSGA-II. J Manuf Syst 2015;36:189–202.

[21] Deb K, Pratap A, Agarwal S, Meyarivan T. A fast and elitist multiobjective genetic algorithm: NSGA-II. IEEE Trans Evol Comput 2002;6:182–97.

[22] Shang C, Srinivasan D, Reindl T. Generation-scheduling-coupled battery sizing of stand-alone hybrid power systems. Energy 2016;114:671–82.

[23] Sorrentino M, Mauramati F, Arsie I, Cricchio A, Pianese C, Nesci W. Application of Willans Line method for internal combustion engines scalability towards the design and optimization of eco-innovation solutions. SAE Technical Paper; 2015.

[24] Rizzoni G, Guzzella L, Baumann BM. Unified modeling of hybrid electric vehicle drivetrains. Mechatronics, IEEE/ASME Transactions on. 1999;4:246–57.

[25] Divya KC, Østergaard J. Battery energy storage technology for power systems—An overview. Electr Power Syst Res 2009;79:511–20.

[26] Xu L, Mueller CD, Li J, Ouyang M, Hu Z. Multi-objective component sizing based on optimal energy management strategy of fuel cell electric vehicles. Appl Energy 2015;157:664–74.

[27] Chen BC, Wu YY, Tsai HC. Design and analysis of power management strategy for range extended electric vehicle using dynamic programming. Appl Energy 2014;113:1764–74.

[28] Onori S, Serrao L, Rizzoni G. Hybrid Electric Vehicles: Springer London; 2016.

[29] Johnson VH. Battery performance models in ADVISOR. J Power Sources 2002;110:321–9.

[30] Holtrop J, Mennen GGJ. An Approximate power prediction method. Int Shipbuild Prog 1982;29:166–70.

[31] Herrera V, Milo A, Gaztañaga H, Etxeberria-Otadui I, Villarreal I, Camblong H. Adaptive energy management strategy and optimal sizing applied on a battery-supercapacitor based tramway. Appl Energy 2016;169:831–45.

[32] Peng J, He H, Xiong R. Rule based energy management strategy for a series–parallel plug-in hybrid electric bus optimized by dynamic programming. Appl Energy 2017;1633–43.

[33] Hung YH, Tung YM, Chang CH. Optimal control of integrated energy management/mode switch timing in a three-power-source hybrid powertrain. Appl Energy 2016;173:184–96.

[34] Wang B, Min X, Li Y. Study on the economic and environmental benefits of different EV powertrain topologies. Energy Convers Manage 2014;86:916–26.

[35] Yang Y, Yang Z, Xu G, Wang N. Situation and prospect of energy consumption for China's thermal power generation. Procee CSEE 2013;1–11.

[36] Edwards R, Mahieu V, Griesemann J-C, Larivé J-F, Rickeard DJ. Well-to-wheels analysis of future automotive fuels and powertrains in the European context. SAE Trans 2004.

[37] Sandmo T. The Norwegian Emission Inventory 2011: documentation of methodologies for estimating emissions og greenhouse gases and long-range transboundary air pollutants; 2011.

[38] Dufo-López R, Bernal-Agustín JL, Mendoza F. Design and economical analysis of hybrid PV–wind systems connected to the grid for the intermittent production of hydrogen. Energy Policy 2009;37:3082–95.

[39] Fellow P, Kaushal N, Hendrickson CT, Peterson SB, Whitacre JF, Michalek JJ. Optimal plug-in hybrid electric vehicle design and allocation for minimum life cycle cost, petroleum consumption, and greenhouse gas emissions. J Mech Des 2010;132:183–95.

[40] Hu C, Youn BD, Chung J. A multiscale framework with extended Kalman filter for lithium-ion battery SOC and capacity estimation. Appl Energy 2012;92:694–704.

[41] Silvaş E, Hofman T, Steinbuch M. Review of optimal design strategies for hybrid electric vehicles. IFAC Procee Vol 2012;45:57–64.

[42] Kalantar M, Mousavi G. SM. Dynamic behavior of a stand-alone hybrid power generation system of wind turbine, microturbine, solar array and battery storage. Appl Energy 2010;87:3051–64.

[43] Sciberras EA, Zahawi B, Atkinson DJ, Juandó A. Electric auxiliary propulsion for improved fuel efficiency and reduced emissions. Procee Instit Mechan Eng, Part M: J Eng Maritime Environ 2015;229:36–44.

[44] Schott JR. Fault tolerant design using single and multicriteria genetic algorithm optimization. Cell Immunol 1995;37:1–13.

[45] AHTS propulsion for swire pacific offshore. < http://marine.man.eu/>; 2015 [accessed 15.12.30].

[46] Diesel M. L27/38-VBS Project Guide. < http://marine.man.eu/four-stroke/engines>; 2015 [accessed 17.05.03].